

Directly probing work extraction from a single qubit engine fueled by quantum measurements

R. Dassonneville,^{1,*} C. Elouard,^{2,†} R. Cazali,¹ R. Assouly,¹ A. Bienfait,¹ A. Auffèves,^{3,4} and B. Huard¹

¹*Ecole Normale Supérieure de Lyon, CNRS, Laboratoire de Physique, F-69342 Lyon, France*

²*Ecole Normale Supérieure de Lyon, Inria, LIP, F-69342, Lyon Cedex 07, France*

³*MajuLab, CNRS-UCA-SU-NUS-NTU International Joint Research Laboratory*

⁴*Centre for Quantum Technologies, National University of Singapore, 117543 Singapore, Singapore*

(Dated: January 29, 2025)

Recent progress in manipulating individual quantum systems enables the exploration of resources of quantum origin in engines. One of the main remaining challenges consists in directly measuring the work extracted from such quantum engines. Here we probe the work extracted from a transmon superconducting qubit acting as a working medium. The engine is fueled by performing quantum measurements of an observable which does not commute with the bare qubit Hamiltonian. Using feedback, the engine acts as a quantum Maxwell demon working without a hot thermal source. In our implementation, the qubit working medium amplifies a coherent microwave field from which work is extracted. The latter is not only inferred from tomographic measurements of the qubit state but also directly monitored via heterodyne detection of the field quadratures. We demonstrate the long-term stability of the engine as well as its robustness to transmon decoherence, losses and drifts. To emphasize the role of feedback, we also study the breakdown of the engine in the open-loop configuration.

I. INTRODUCTION

Identifying and harnessing quantum signatures in non-equilibrium thermodynamics is a task that is currently gathering a lot of attention. Quantum engines [1] are paradigmatic machines designed to explore the thermodynamic impact of quantum resources - such as coherent superposition or entanglement - as well as of quantum processes triggering energy exchanges. In this context, the inherent backaction of measurements on the state of a quantum system offers a unique tool for manipulating energy flows. When the measured observables do not commute with the system Hamiltonian, the resulting backaction modifies the system average energy, behaving as a non-classical energy resource [2–6]. This principle allows for the design of quantum engines that have no classical equivalent by incorporating quantum measurements into their thermodynamic cycles. Many engines have been proposed in order to exploit measurement-induced energy transfers, where they play a role similar to the heat from a hot bath, injecting both energy and entropy in the system, to perform work extraction [7, 8]: engines exploiting the coherence of a single qubit requiring a feedback step [9–12] or not [13–15], non-commuting successive measurements [16, 17], continuous monitoring [18, 19], general quantum measurements [20, 21], or entanglement in two or multi qubit systems [22–25]. Previous experiments with optical [26, 27] and NMR setups [28, 29] have demonstrated the feasibility of such engines, for which the work output was inferred from the

observed dynamics of the quantum state of the working agent. However, a key challenge remains: directly probing the extracted work itself in a measurement-fueled engine.

Superconducting circuits are highly controllable systems, making them an ideal testbed for quantum energetics and quantum thermodynamics [5, 30–40]. In particular, it is possible to measure the microwave pulses driving the qubit with high efficiency, providing access to the energy changes stemming from the interaction with the qubit [36]. Building on this capacity, we report the direct probing of the extracted work in a quantum engine powered by measurements. Following a proposal by some of us [10], our engine utilizes a single superconducting qubit. On the one hand, the qubit, as a working medium, exchanges power with a resonant microwave propagating field along cycles of stimulated emissions and absorptions. On the other hand, the qubit is periodically measured in a basis which does not commute with its bare Hamiltonian, giving rise to an input of energy and entropy with no classical equivalent. Exploiting the measurement outcomes in a feedback loop allows us to extract some net power in the output field, that we directly probe. Our results provide a new realization of a quantum Maxwell demon, where the hot source is replaced by the measurement channel. We verify that not exploiting the measurement outcomes (open loop configuration) leads to the engine switching off. Fast measurement rates delay the switching off, which is consistent with the Zeno regime where the measurement backaction is deterministic.

The article is structured as follows. In Section II, we detail the principle of the engine and its physical implementation. Then in Section III, we exhibit the correspondence between the tomographic evolution of the qubit state and the extracted work and showcase the en-

* Current address: Aix Marseille Université, Université de Toulon, CNRS, IM2NP, Marseille, France

† Current address: Université de Lorraine, CNRS, LPCT, F-54000 Nancy, France

gine switching off when the Maxwell demon is rendered inactive. Finally, in Section IV, we study the work extraction's performance as a function of the driving Rabi amplitude and duration.

II. PRINCIPLE OF THE ENGINE AND EXPERIMENTAL IMPLEMENTATION

Our engine produces work by converting the energy change of a superconducting transmon qubit upon the backaction of a measurement of $\hat{\sigma}_x = |-z\rangle\langle+z| + |+z\rangle\langle-z|$, which does not commute with the qubit Hamiltonian $\hbar\omega_q\hat{\sigma}_z/2 = \hbar\omega_q(|+z\rangle\langle+z| - |-z\rangle\langle-z|)/2$ [2]. The extracted work is used to amplify a propagating coherent microwave mode that here plays the role of a battery. As shown in Fig. 1.a, the engine operates a 3-stroke cycle after an initialization step [10].

We now detail the experimental implementation of each step and the measurement of the work output (see Fig. 1.b-c and Appendices A and D for more details). The initialization step ① is achieved by an active reset of the qubit in its ground state $|-z\rangle$, followed by a pulse $+\pi/2$. Active reset is performed by applying a π pulse to the qubit until it is read out in its ground state. At the end of step ①, the qubit thus starts in the state $|+x\rangle$ with an average internal energy $\hbar\omega_q/2$ with frequency $\omega_q/2\pi = 4.983$ GHz.

In step ②, the qubit is resonantly driven by a square pulse for a time t_R , with an average Rabi frequency Ω . The drive rotates the qubit state by an angle $\theta = \Omega t_R$ around the y -axis of the Bloch sphere, changing its average internal energy by $-\hbar\omega_q \sin(\theta)/2$. This energy is coherently added to the driving pulse via stimulated emission and absorption, which constitutes the work extraction of the engine. The Rabi drive is achieved through the capacitive coupling of the qubit to a transmission line at a rate $\Gamma_c/2\pi = 0.383$ kHz. From the input/output relations [41], the field that describes the outgoing pulse \hat{b}_{out} is related to the input field \hat{b}_{in} and the qubit state as $\hat{b}_{out}(t) = \hat{b}_{in}(t) + \sqrt{\Gamma_c}\hat{\sigma}_-(t)$. The average power $P_{out}(t)$ outgoing from the qubit at time t is then given by [42–44]

$$\begin{aligned} \frac{P_{out}(t)}{\hbar\omega_q} &= \langle \hat{b}_{out}^\dagger(t)\hat{b}_{out}(t) \rangle \\ &= \langle \hat{b}_{in}^\dagger(t)\hat{b}_{in}(t) \rangle + \frac{\Omega}{2} \langle \hat{\sigma}_x(t) \rangle + \Gamma_c \frac{1 + \langle \hat{\sigma}_z(t) \rangle}{2} \\ &= \frac{P_{in}(t)}{\hbar\omega_q} + \frac{\Omega}{2} \langle \hat{\sigma}_x(t) \rangle + \Gamma_c \frac{1 + \langle \hat{\sigma}_z(t) \rangle}{2}, \end{aligned} \quad (1)$$

where $\Omega = 2\sqrt{\Gamma_c} \left| \langle \hat{b}_{in} \rangle \right|$ is the Rabi frequency and $P_{in}(t)$ is the average input power. The term $\Omega \langle \hat{\sigma}_x(t) \rangle / 2$ corresponds to coherent stimulated emission or absorption, while the term $\Gamma_c(1 + \langle \hat{\sigma}_z(t) \rangle) / 2$ corresponds to incoherent emission. In the limit $\left| \langle \hat{b}_{in} \rangle \right| \gg \sqrt{\Gamma_c}$, incoherent emission can be neglected and the excess power is directly given by the product of half the Rabi frequency

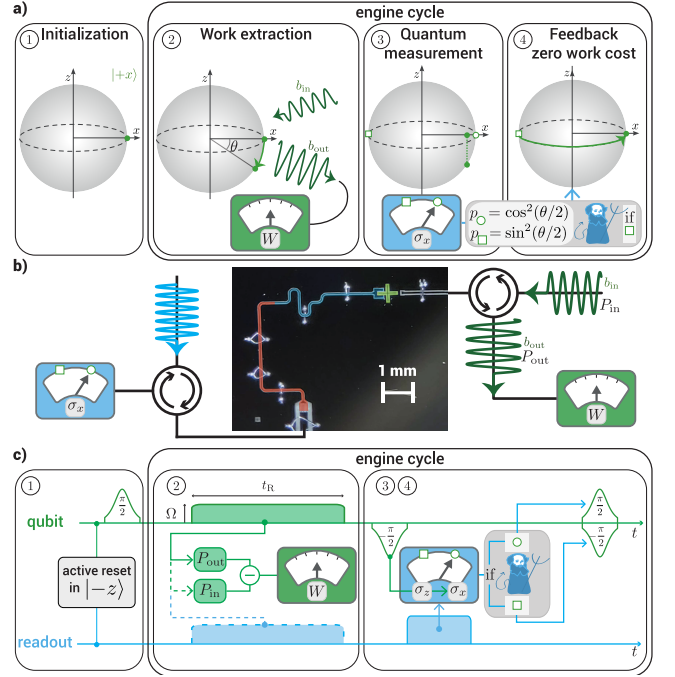


FIG. 1. A measurement-powered quantum engine: a) in ①, the qubit is initialized in state $|+x\rangle$. In ②, the qubit is resonantly driven. The outgoing field acquires an excess of power compared to the incoming field thanks to stimulated emission, and useful work can be extracted in the outgoing field. In ③, the qubit is projectively measured in its $\hat{\sigma}_x$ basis. In ④, depending on the outcome of the readout, the qubit is actively reinitialized in $|+x\rangle$ and the thermodynamic cycle restarts at ②. b) Simplified schematic of the setup with an optical image of the superconducting circuit in false colors. A transmon qubit (green) can be directly driven and its outgoing field is measured via heterodyne detection. The qubit state is readout via its dispersive interaction with a resonator (blue). A Purcell filter (red) limits the qubit decay through the readout resonator. c) Pulse sequence implementing the engine: the qubit is initialized in $|+x\rangle$ via a $\pi/2$ -pulse after a measurement-based active reset in $|-z\rangle$. We measure the output power P_{out} during the Rabi drive of amplitude Ω and duration t_R . The useful work is given by $W = (P_{out} - P_{in})t_R$ where P_{in} (dash lines) is calibrated by detuning the qubit using the AC Stark effect (see Appendix D). The qubit-readout dispersive interaction gives a QND-measurement of $\hat{\sigma}_z$. It is transformed into a QND $\hat{\sigma}_x$ measurement by applying a $-\pi/2$ pulse before and a $+\pi/2$ pulse after the readout pulse. If the qubit is measured in the $|-x\rangle$ state, a $-\pi/2$ pulse is applied instead of the $+\pi/2$ thanks to FPGA-based real-time feedback.

$\Omega/2$ by the coherence $\langle \hat{\sigma}_x(t) \rangle$ of the qubit. Over the duration t_R of the drive, the average internal energy of the qubit decreases by $\hbar\omega_q \sin(\theta)/2$, corresponding to the extracted work of the operation. For $\theta \leq \pi \bmod 2\pi$, the extracted work is positive. It stems from the positive balance between stimulated emission and absorption. To get a sense of the average power levels we need to resolve, a Rabi rate $\Omega/2\pi$ between 1 kHz and 1 MHz would produce

an excess power $P = P_{\text{out}} - P_{\text{in}}$ of at best $\Omega\hbar\omega_q/2$, which is between 10zW and 10aW for our qubit frequency.

In step ③, the qubit is read out in its $\{|+x\rangle, |-x\rangle\}$ basis, yielding the outcome $\pm x$ with probabilities $\cos^2(\theta/2)$ and $\sin^2(\theta/2)$. Whatever the outcome, the measurement deterministically restores the qubit internal energy to its initial value $\hbar\omega_q/2$. In the interpretation of the engine as a Maxwell demon, the measurement can be decomposed in two effects. Its backaction provides energy to the qubit and would also increase its entropy if the outcome was discarded. It therefore plays the role of a hot bath. On the flip side, the information it brings cancels the entropy increase. It corresponds to the demon storing the information into its memory. Here, we experimentally implement a quasi Quantum-Non-Demolition (QND) readout of $\hat{\sigma}_x$ by sequentially performing first a $-\pi/2$ gate on the qubit, followed by a single shot dispersive readout in the $\{|+z\rangle, |-z\rangle\}$ basis and finally a $\pi/2$ gate (see Appendix B). The first $-\pi/2$ pulse maps the basis $\{|-z\rangle, |+z\rangle\}$ onto the $\{|+x\rangle, |-x\rangle\}$ basis, while the second $\pi/2$ reverses the operation.

In the fourth and last step ④, the qubit is reset to its initial state $|+x\rangle$ whatever the outcome $\pm x$ of the readout. A feedback pulse is applied if and only if the readout outcome is $-x$ (*i.e.*, the Maxwell demon prepares the state for next cycle's work extraction). As the qubit internal energy is not changed during the feedback step, this Z gate step has no extra energy cost. Experimentally, it is more efficient to merge the Z rotation with the measurement protocol of step ③: When the outcome $-x$ is obtained, the $+\pi/2$ gate ending step ③ is replaced with a $-\pi/2$ mapping $\{|-z\rangle, |+z\rangle\}$ onto $\{|-x\rangle, |+x\rangle\}$, while for $+x$, the $+\pi/2$ is conserved. This feedback operation is performed using Quantum Machines' FPGA-based control system (OPX), and introduces a delay which cannot be reduced below 200 ns.

The complete thermodynamic cycle of the measurement engine involves the reset of the memory of the measuring apparatus [10]. Here, the memory corresponds to the readout resonator, that leaks out quickly during step ③ with the characteristic timescale $\kappa^{-1} \sim 18$ ns. Note that this reset corresponds to a Landauer's erasure at no work cost, the memory's entropy being dumped in a zero temperature bath. The steps ②-④ can therefore be operated cyclically to generate sustained work extraction.

To measure directly the extracted work flow which can be as low as tens of zW, the driving Rabi pulse is reflected and amplified using a Traveling Wave Parametric Amplifier (TWPA) [45]. A calibrated heterodyne measurement yields a continuous record of the two quadratures of the outgoing field $\hat{b}_{\text{out}}(t)$ (see Appendix D). From the heterodyne measurement, we access the instantaneous power $P_{\text{out}}(t)/\hbar\omega_q = \langle \hat{b}_{\text{out}}^\dagger(t)\hat{b}_{\text{out}}(t) \rangle \simeq \left| \langle \hat{b}_{\text{out}}(t) \rangle \right|^2$ outgoing from the qubit port [36] (step ② in Fig. 1.c). The extracted work flow can be obtained by measuring the instantaneous excess power $P(t) = P_{\text{out}}(t) - P_{\text{in}}(t)$, where we calibrate the input power using sequences where the

qubit is shifted out of resonance through the AC-Stark effect (see Appendix C). In that case, the heterodyne detection gives us access to the instantaneous quadratures of the incoming field $\hat{b}_{\text{in}}(t)$ and thus the instantaneous input power $P_{\text{in}}(t)/\hbar\omega_q = \langle b_{\text{in}}^\dagger b_{\text{in}}(t) \rangle \simeq \left| \langle \hat{b}_{\text{in}}(t) \rangle \right|^2$. The measurements of P_{out} and P_{in} are interleaved to mitigate as much as possible the detrimental effects of experimental drifts over time.

III. CHARACTERIZATION OF THE CYCLIC EVOLUTION, THE IMPORTANCE OF FEEDBACK

We perform the tomography of the qubit state as well as direct measurement of the excess power $P(t)$ within the first three cycles after initialization (Fig. 2). These characterizations are here performed for $t_R = 8 \mu\text{s}$, $\Omega/2\pi = 14.2$ kHz and averaged over hundreds of thousand of repetitions for $P(t)$. We observe that the qubit follows the same in-cycle trajectory in the Bloch sphere for all three cycles. Due to the relatively long drive duration t_R compared to the finite coherence times T_1 and T_2 , the qubit does not stay on the surface of the Bloch sphere within a cycle and thus is not fully captured by the Rabi angle θ . However, just considering the finite T_1 and T_2 of the qubit is not enough to reproduce the experimental qubit trajectory during step ② as spurious fluctuations of the qubit frequency and qubit coherence times must also be included (see Appendix J). The measured instantaneous excess powers $P(t)$ are identical for each cycle and match the power due to stimulated absorption and emission computed from the qubit's tomography $\hbar\omega_q\Omega \langle \hat{\sigma}_x(t) \rangle / 2$. We expect the small deviations to be due to the slow drift of qubit parameters over time. As the tomography measurements take less averaging and thus less time than the direct measurement of the power P , they are less prone to drifts. This deviation reveals the importance of the direct measurement of the excess power to truly characterize the engine performance.

For the sake of comparison, we also performed the qubit tomography and engine power measurement in the case of the wrong open-loop configuration by purposely setting off the feedback step ④. It is realized by always performing a $+\pi/2$ pulse whatever the readout outcome with the same delays as when the feedback is on. In that case, the cycles are not equivalent to each other (Fig. 2). Assuming an ideal qubit with no decoherence, as the randomness of the measurement-induced dynamics effectively produces the mixed qubit state $\rho^{(N_c)} = p_+^{(N_c)} |+x\rangle\langle+x| + p_-^{(N_c)} |-x\rangle\langle-x|$ at the end of the N_c -th cycle, with $p_\pm^{(N_c)} = [1 \pm \cos^{N_c}(\theta)]/2$, the qubit state gets closer to the center of the Bloch sphere after each cycle. The excess power $P^{(N_c)} = \frac{\hbar\omega_q\Omega}{2} \cos^{N_c}(\theta)$ thus tends to zero with the number of cycles. Power could still be extracted for numerous cycles in the small angle limit $\theta \rightarrow 0$, where the excess power at cycle N_c is given

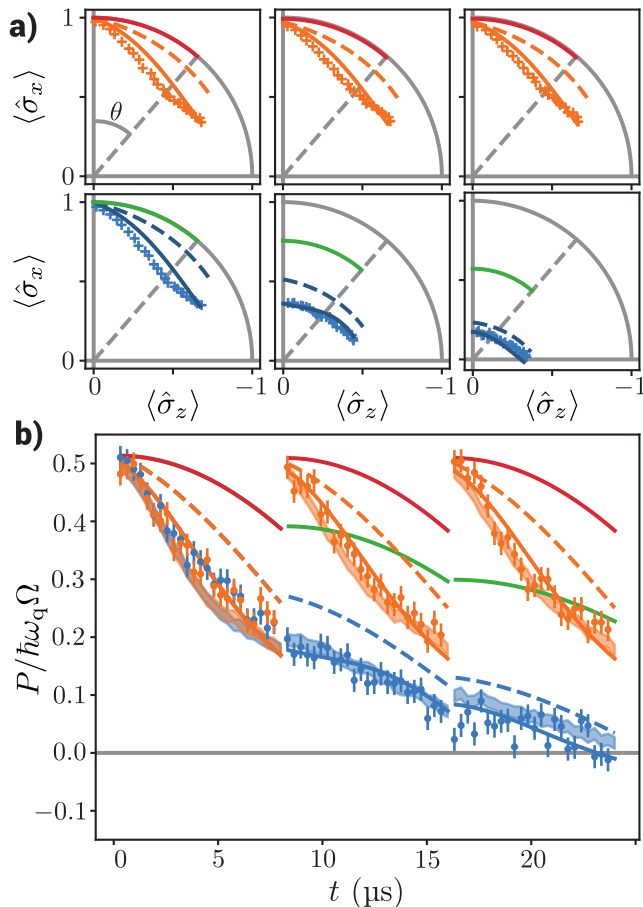


FIG. 2. a) Measured Bloch coordinates $\langle \hat{\sigma}_x(t) \rangle$ as a function of $\langle \hat{\sigma}_z(t) \rangle$ during the first three cycles of the engine from left to right (top, in orange) or in the open-loop configuration without feedback (bottom, in blue). Dots with errorbars are the measured excess power $P/\hbar\omega_q\Omega$. Shadows are the measured $\langle \hat{\sigma}_x(t) \rangle / 2$ assuming a 1% errorbar due to gate and readout infidelities. In a-b), $\Omega/2\pi = 14.2$ kHz, $t_R = 8 \mu\text{s}$. Solid red (green) lines correspond to the cases of infinite T_1 and T_2 and resonant drive of the (open-loop) engine. Dash lines are master equation simulations assuming resonant drive, $T_1 = 25 \mu\text{s}$ and $T_2 = 32 \mu\text{s}$, while solid lines are simulation assuming fluctuating qubit frequency and T_2 (see Appendix J and Appendix G). Note that the visible dead times of 536 ns correspond to the duration t_{meas} of steps 3 and 4.

by $P^{(N_c)} \simeq \frac{\hbar\omega_q\Omega}{2}(1 - \frac{N_c\theta^2}{2})$. This corresponds to the Zeno limit where a strong $\hat{\sigma}_x$ measurement “freezes” the qubit in its $|+x\rangle$ state, making measurement back-action deterministic, and the feedback of the Maxwell demon unnecessary [10]. However, the limited coherence time T_2 of the qubit prevents the observation of this regime as it is not much larger than the duration of the measurement of $\hat{\sigma}_x$ (see Appendix I). Interestingly, due to the finite coherence times, the open-loop configuration can present a non-zero extracted work in the steady-state, especially when t_R is a non-negligible fraction of T_1 and T_2 . For instance, in the case of $t_R = 8 \mu\text{s}$ and $\Omega/2\pi = 20.2$ kHz, we observe, in the steady state, a negative excess power

of about -0.02 aW, which is absorbed on average by the qubit which ends up closer to $| -x \rangle$ than $| +x \rangle$ at the end of each cycle (see Fig. 8).

IV. EXTRACTED WORK VERSUS RABI ANGLE

Integrating the instantaneous power $P(t)$ over the drive duration t_R within each cycle, we obtain the average extracted work over one cycle $W(N_c) = \int_{t=(N_c-1)t_R}^{t=N_ct_R} P(t)dt$, which we observe to be, as expected, a constant of the cycle number N_c (see Appendix H). We further study the performance of the engine (feedback on) by plotting the work \bar{W} averaged over 40 cycles as a function of Ω and t_R (see Fig. 3). In the ideal case of infinite lifetimes, the normalized extracted work $\bar{W}/\hbar\omega_q t_R \Omega$ is given by $\text{sinc}(\theta)/2$ [10]. In the small angle limit $\theta \ll 1$, work extraction is maximized to $\bar{W} = \hbar\omega_q t_R \Omega / 2$ as the qubit stays close to the state $|+x\rangle$ where $\langle \hat{\sigma}_x \rangle = 1$. This small angle limit experimentally requires the condition $T_2 \gg \Omega^{-1} \gg t_R \gg t_{\text{meas}}$, resulting in, for our device, $\sim 30 \mu\text{s} \gg \Omega^{-1} \gg t_R \gg 536$ ns. For each drive duration t_R in [2, 4, 6, 8, 16] μs , we vary the Rabi angle $\theta = \Omega t_R$ by sweeping the Rabi rate Ω from 3.4 kHz to 227 kHz. We observe the expected sinc oscillations of the normalized extracted work as a function of θ . As the driving duration t_R becomes a non-negligible fraction of T_2 , the qubit’s entropy increases within each cycle, and the amplitude of the extracted work diminishes: it is then given by $\bar{W}/\hbar\omega_q\Omega = \frac{1}{2} \int_0^{t_R} \cos(\Omega t) e^{-t/T_2} dt$.

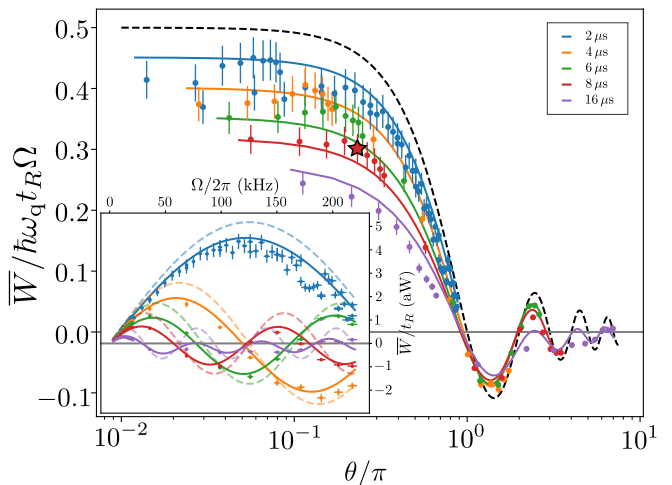


FIG. 3. Dots: normalized extracted work per cycle $\bar{W}/\hbar\omega_q t_R \Omega$ averaged over 40 cycles as a function of Rabi angle $\theta = \Omega t_R$ (simulation in solid lines). For a qubit with an infinite long lifetime and resonant driving, the normalized work is given by $\text{sinc}(\theta)/2\theta$ (dash line). The star highlights the parameter space as in Fig. 2. Inset: extracted work flow \bar{W}/t_R in aW as a function of Rabi rate Ω . The different colors correspond to different durations t_R (see legend).

As in the case for the data of the tomographic qubit state evolution (Fig. 2.a), we have to consider the fast changes and drifts of the qubit parameters over time (see Appendix J). The change of qubit frequency is quite detrimental for the engine's operation as a resonant Rabi drive is assumed and required. Indeed, the detuning $\Delta = \omega_d - \omega_q$ of the drive will not only increase the Rabi rate as $\Omega' = \sqrt{\Omega^2 + \Delta^2}$ but also shift the rotation axis. A more complex trajectory on the Bloch sphere is then expected if there is an uncontrolled detuning Δ during the Rabi drive duration t_R , which might even result in negative extracted work. We simulate the extracted work by assuming that the qubit takes only a few discrete values of ω_q and T_2 due to its coupling to uncontrolled two-level-systems (TLS) [46]. To estimate this effect, we have measured afterward the qubit parameters ω_q , T_1 and T_2 as a function of time with relaxation and Ramsey measurements. For the simulations, we assume a simplified model with two main TLS, one shifting the qubit frequency by 70 kHz with $T_1 = 25.4 \mu\text{s}$ and $T_2 = 34 \mu\text{s}$, and the other one shifting the qubit frequency by 6 kHz and reducing the coherence to $T_2 = 21 \mu\text{s}$. The only fitting parameters are then the fraction of time spent in one of the two states of each TLS. Under these assumptions, the extracted work \bar{W} as a function of Ω and t_R is well reproduced.

V. CONCLUSION

We have successfully demonstrated the operation of an engine solely powered by quantum measurement backaction and probed its performance via direct measurement of the extracted work. We have linked the qubit tomography to the excess power within a cycle and as a function of cycle number. We have identified two primary limitations of performance in the demonstrated quantum measurement engine: first, the frequency stability of the qubit over time, and second, its finite coherence time. Such limitations may be mitigated with better optimization of the superconducting qubit fabrication. Moreover, the $\hat{\sigma}_x$ readout outcomes over several successive cycles may be used to estimate the qubit detuning and stabilize the qubit frequency during the engine operation with ac-Stark effect or using a flux-tunable qubit [47].

Our current focus has been on measuring the average extracted work. However, in future studies, investigating the full statistics of work fluctuations through single-shot measurements would be of great interest, especially in the context of quantum fluctuation theorems [48, 49] and thermodynamic/kinetic uncertainty relations [50–53]. Achieving this would require work measurement with high quantum efficiency and high resolution, such as employing high-efficiency heterodyne detection [54], microwave photon detectors or counters [55–57] or bolometers and calorimeters [58]. The reflection of the relatively large incoming drive may be challenging to handle. This issue can be mitigated by using non-resonant gates

and/or Rabi drives such as subharmonic driving [59] in order to separate the incoming field from the outgoing field in frequency.

Superconducting quantum circuits, enabling high-fidelity QND measurements and feedback schemes, present a state-of-the-art platform for investigating the thermodynamic costs of quantum information processing, particularly in studying the performance and limitations of quantum measurement engines with different cycling strategies [7, 9–25]. Advancing the study of quantum measurement engines will not only improve our understanding of the thermodynamic costs and energy efficiency of quantum information processors [60–65], but also shed light on different interpretations of quantum mechanics [8].

ACKNOWLEDGMENTS

We acknowledge IARPA and Lincoln Labs for providing a Josephson Traveling-Wave Parametric Amplifier. A.A. acknowledges the National Research Foundation, Singapore and A*STAR under its CQT Bridging Grant, the ANR Research Collaborative Project “Qu-DICE” (Grant No. ANR-PRC-CES47), the Foundational Questions Institute Fund (Grant No. FQXi-IAF19-01 and Grant No. FQXi-IAF19-05) and the John Templeton Foundation (Grant No. 61835). We thank Guillaume Cauquil, Maria Maffei, and Antoine Marquet for useful discussions.

Appendix A: Sample and measurement setup

The large features of the circuit are made by optical lithography on a Tantalum thin film deposited on a Sapphire substrate. The readout mode is a $\lambda/4$ coplanar waveguide resonator. The Purcell filter is also a $\lambda/4$ coplanar waveguide resonator, with frequency close to and inductively coupled to the readout mode. It is used as a bandpass filter around the readout frequency and limits the qubit decay through the readout resonator line. The Josephson junction of the transmon qubit is fabricated using electronic lithography followed by angle deposition of Al/AlO_x/Al in a Plassys evaporator.

The sample is cooled down to 10 mK in a dilution refrigerator. The diagram of the microwave wiring is given in Fig. 4. The microwave pulses are generated by modulation of continuous microwave tones produced respectively by generators Anapico APSIN20G and Anapico APSIN12G (all qubit-type tones use the same local oscillator). They are modulated via IQ-mixers where the intermediate frequency (a few tens of MHz) modulation pulses are generated by 8 DAC channels of an OPX from Quantum Machines with a sample rate of 1 GS/s. Two channels are used for the readout operation, while the 6 others used for the qubit operation are separated into 3 sets of 2, namely, qubit Rabi, qubit gate and qubit gate

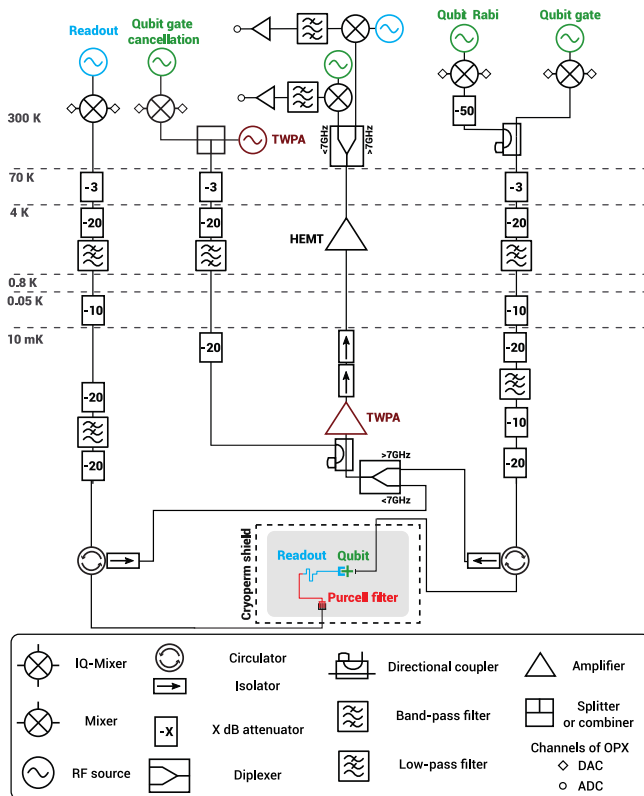


FIG. 4. Schematic of the microwave wiring. The Josephson Traveling Wave Parametric Amplifier (TWPA) was provided by the Lincoln Lab. The RF source colors refer to the frequency of the matching element in the device up to a modulation frequency. Identically colored sources represent a single instrument with a split output.

cancellation. The qubit Rabi and qubit gate pulses are sent into a single transmission line using a directional coupler. The qubit gate is used to generate the fast π and $\pi/2$ qubit gate pulses while the qubit Rabi is used to generate the longer drive at amplitude Ω and duration t_R with a square envelope. Due to the large dynamical range (around 70 dB difference) required between qubit gate and qubit Rabi pulses, we used two different IQ-mixers and 4 DAC channels instead of just one IQ-mixer and 2 DAC channels. Moreover, another set of two DAC channels has to be added in order to reduce nonlinear effects such as saturation in the output amplification chain (see below).

The readout and qubit Rabi outgoing pulses are multiplexed into a single output transmission line using a diplexer at the lowest temperature stage. The readout and qubit signals are then amplified with at first a quantum-limited parametric amplifier (a Travelling-Wave Parametric Amplifier, TWPA from Lincoln Lab) and then by a HEMT amplifier. At room temperature, the readout and qubit Rabi signals are separated using a diplexer. Each signal is acquired, after down-conversion by its local oscillator, by digitizing at 1 GS/s with one of the two ADCs of the OPX.

In principle, the qubit gate pulses could also be acquired through the same ADC as the qubit Rabi signal. Qubit gate and qubit Rabi signals could be distinguished as they are separated in time during the pulse sequence. However, due to the large power difference between the gate and Rabi pulses, the Rabi detection was impaired. In order to not disturb the amplification chain with the high-power gate pulses, we have added a gate cancellation tone at the input of the TWPA (see Fig. 4). This tone is calibrated to destructively interfere with the reflected qubit gate $\pi/2$ pulses. We then recalibrate our gate pulses with the corresponding applied cancellation gate pulses, as the latter leak towards the qubit with an attenuated power by ~ 60 dB.

The transmon qubit has a frequency $\omega_q/2\pi = 4.983$ GHz and anharmonicity of -221 MHz. It is coupled to a $\lambda/4$ coplanar waveguide (CPW) readout resonator of frequency $\omega_r/2\pi = 7.665$ GHz, resulting in the dispersive interaction $\hat{H}/\hbar = -\chi/2 \hat{r}^\dagger \hat{r} \hat{\sigma}_z$ with coupling rate $\chi/2\pi = 3.3$ MHz where \hat{r} is the annihilation operator of the readout resonator. The readout resonator is also coupled to a $\lambda/4$ CPW bandpass Purcell filter, resulting in a readout decay rate $\kappa/2\pi = 9$ MHz. The Purcell filter is intended to limit the qubit decay through the port used to probe the readout resonator. The qubit is capacitively coupled to its transmission line at a rate $\Gamma_c/2\pi = 0.383$ kHz. This line is used to excite the qubit but also directly measure its emitted power, which contains the work extracted by the engine. The qubit presents a total relaxation time $T_1 = 25.4 \pm 0.5$ μ s and dephasing time T_2 varying from 10 μ s to 45 μ s over a few days. It is thus not Purcell-limited by its direct coupling to the transmission line (Purcell limit of 416 μ s).

Appendix B: Qubit state readout

A quasi-QND readout of $\hat{\sigma}_z$ is obtained in 280 ns integration time with single-shot readout fidelity of $F = 1 - [P_{|-z\rangle}(+z) + P_{|+z\rangle}(-z)]/2 = 98.5\%$ where $P_{|a\rangle}(b)$ is the probability to obtain the outcome b when having prepared state $|a\rangle$. These probabilities are extracted from histograms of single-shot readouts, where the ground state $|-z\rangle$ is identified by having an outcome α in the top left part ($\text{Re}\{\alpha\} < 0$ and $\text{Im}\{\alpha\} > 0$) of the complex IQ plane while the excited state $|+z\rangle$ is identified as being in the top right part ($\text{Re}\{\alpha\} \geq 0$ and $\text{Im}\{\alpha\} > 0$). Such readout histograms are shown in Fig. 5 after having prepared the ground or the excited state. From the readout histograms of the thermal equilibrium state, we roughly estimate the qubit to be at an equilibrium temperature of 54 mK, as the qubit has a thermal population around 1%. Moreover, we have a probability $P_{|-z\rangle}(\pm z) \sim 0.1\%$ and $P_{|+z\rangle}(\pm z) \sim 0.2\%$ of not reading out the ground or excited state due to readout ionisation of the transmon out of its qubit subspace [66–68]. This 0.15% error on average is not considered in the feedback protocol of our engine, where the transmon qubit will be assumed to only

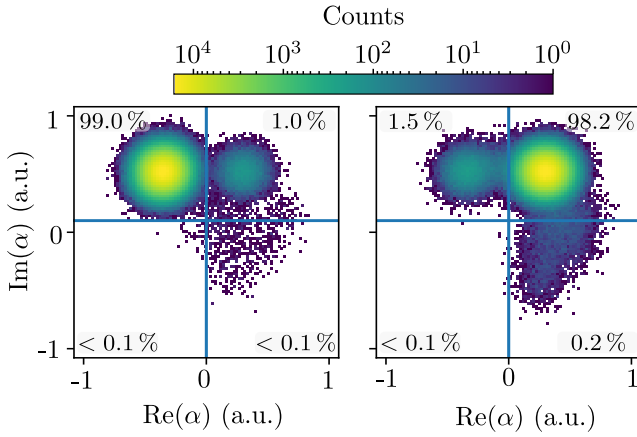


FIG. 5. Qubit state readout: histograms of the readout quadratures when the qubit has been prepared in its thermal equilibrium state (close to its ground state $| -z \rangle$ in the left panel) or after a π -pulse from its thermal equilibrium state (close to its excited state $| +z \rangle$).

be in its ground state if $\text{Re}\{\alpha\} < 0$ or in its excited state if $\text{Re}\{\alpha\} \geq 0$. We expect that it would lead to a small renormalization of the measured work.

As explained in the main text, this $\hat{\sigma}_z$ readout is transformed into a $\hat{\sigma}_x$ readout by applying a $-\pi/2$ -pulse and then applying afterwards a $+\pi/2$ pulse. The $\pm\pi/2$ -pulses used in the engine cycle and the π pulses used in the qubit active reset have a hyperbolic secant temporal envelope whose width is $\sigma = 8$ ns and which is truncated at 4σ . On previous cool downs, with the same sample, the qubit demonstrating a reduced T_2 of $7.5 \mu\text{s}$ had coherence-limited gate infidelities of 0.16% measured by randomized benchmarking [69].

Appendix C: AC-Stark shift and measurement-induced dephasing

To characterize the couplings κ and χ but also to calibrate the AC-Stark effect, we performed measurement-induced dephasing through a Ramsey-like pulse sequence [70]. The induced frequency shift ω_{AC} and dephasing Γ_{AC} are given by

$$\begin{aligned}\Gamma_{\text{AC}} &= \chi \text{Im}\{\alpha_{-z}^* \alpha_{+z}\} \\ \omega_{\text{AC}} &= \chi \text{Re}\{\alpha_{-z}^* \alpha_{+z}\}\end{aligned}\quad (\text{C1})$$

where $\alpha_{-z} = \epsilon/(\kappa/2 - i(\delta\omega - \chi/2))$ and $\alpha_{+z} = \epsilon/(\kappa/2 - i(\delta\omega + \chi/2))$ are the readout resonator coherent steady-state when the qubit is in state $| -z \rangle$ or $| +z \rangle$ respectively. The driving amplitude ϵ and detuning $\delta\omega = \omega_r - \omega_d$ between the driving frequency ω_d and the readout resonator frequency ω_r . They are displayed in Fig. 6 for different input amplitudes. The fit using Eq. (C1) allows us to calibrate the attenuation factor between the room temperature amplitude and ϵ but also to extract the rates

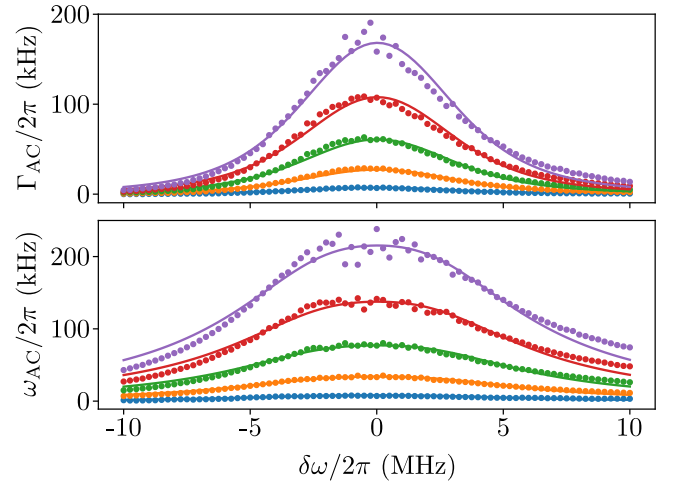


FIG. 6. Measurement-induced dephasing Γ_{AC} and AC-Stark shift ω_{AC} as a function of the detuning $\delta\omega$ of the driving tone compared to the readout resonator frequency. Experimental data in dots and fit using Eq. (C1) in solid line. The different colors correspond to different driving amplitudes, resulting in an average photon number at zero detuning of $3 \cdot 10^{-3}$ in blue, $1.3 \cdot 10^{-2}$ in orange, $3 \cdot 10^{-2}$ in green, $5.3 \cdot 10^{-2}$ in red, and $8.3 \cdot 10^{-2}$ in purple.

$\chi/2\pi = 3.3$ MHz and $\kappa/2\pi = 9$ MHz. During the engine calibration sequence to measure P_{in} , the qubit is shifted by $\omega_{\text{AC}}/2\pi = 1$ MHz (and $\Gamma_{\text{AC}}/2\pi = 0.14$ MHz) with the calibrated driving amplitude at a detuning of $\delta\omega/2\pi = -10$ MHz.

Appendix D: Calibration of the measured power

With our heterodyne measurement setup, the field that we are measuring is not \hat{b}_{out} but the field \hat{B}_{out} after the output amplification line following

$$\hat{B}_{\text{out}} = \sqrt{G}\hat{b}_{\text{out}} + \sqrt{G-1}\hat{i}_{\text{out}}^\dagger \quad (\text{D1})$$

where G is the total gain of the output line and \hat{i}_{out} is an effective idler mode, that captures the addition of noise of phase-preserving amplification. The output power is thus given by

$$\begin{aligned}\langle \hat{B}_{\text{out}}^\dagger \hat{B}_{\text{out}} \rangle &= G \left(|\beta_{\text{in}}|^2 + \Gamma_c \frac{1 + \langle \sigma_z \rangle}{2} + \frac{\Omega}{2} \langle \sigma_x \rangle \right) \\ &+ (G-1) \langle \hat{i}_{\text{out}} \hat{i}_{\text{out}}^\dagger \rangle.\end{aligned}\quad (\text{D2})$$

and

$$\begin{aligned}\langle \hat{B}_{\text{in}}^\dagger \hat{B}_{\text{in}} \rangle &= G (|\beta_{\text{in}}|^2) \\ &+ (G-1) \langle \hat{i}_{\text{out}} \hat{i}_{\text{out}}^\dagger \rangle.\end{aligned}\quad (\text{D3})$$

From the measured quadratures $\langle \hat{B}_{\text{in/out}}(t) \rangle$ and calibrations of the gain G for the different sets of measure-

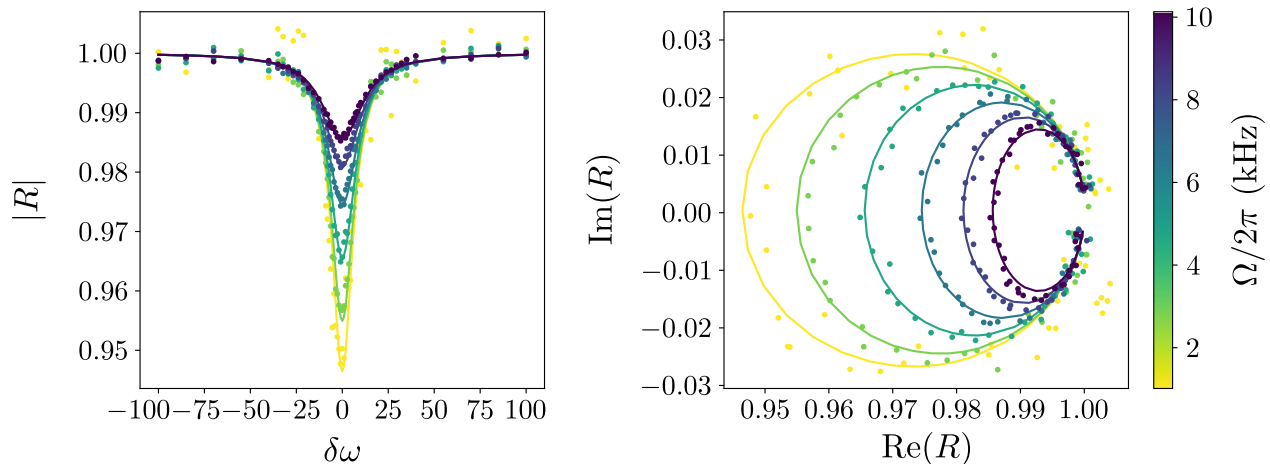


FIG. 7. Amplitude (a) and polar representation (b) of the qubit reflection coefficient R as a function of detuning $\delta\omega = \omega_q - \omega_d$ between the drive ω_d and the qubit frequency ω_q for various drive amplitudes, i.e. various Rabi rate Ω . Dots: measured and solid lines: fits using Eq. (E1).

ments, we compute the excess power

$$\begin{aligned} \frac{P_{\text{out}}(t) - P_{\text{in}}(t)}{\hbar\omega_q} &= \langle \hat{b}_{\text{out}}^\dagger(t) \hat{b}_{\text{out}}(t) \rangle - \langle \hat{b}_{\text{in}}^\dagger(t) \hat{b}_{\text{in}}(t) \rangle \\ &\simeq \frac{|\langle \hat{B}_{\text{out}}(t) \rangle|^2 - |\langle \hat{B}_{\text{in}}(t) \rangle|^2}{G} \quad (\text{D4}) \end{aligned}$$

Appendix E: Calibration of the coupling rate Γ_c

The rate Γ_c characterizes the coupling rate of the qubit with the transmission line. We determine it by measuring the reflection coefficient $R = \frac{\langle \hat{b}_{\text{out}} \rangle}{\langle \hat{b}_{\text{in}} \rangle}$ of the qubit [36]

$$R(\delta) = 1 - (p_{|-z\rangle}^{\text{th}} - p_{|+z\rangle}^{\text{th}}) \frac{\Gamma_c \Gamma_1 (\Gamma_2 - i\delta)}{[\Gamma_1 (\Gamma_2^2 + \delta^2) + \Gamma_2 \Omega^2]}, \quad (\text{E1})$$

where $\Gamma_1 = 1/T_1$, $\Gamma_2 = 1/T_2$, $\delta\omega = \omega_q - \omega_d$. The thermal population $p_{|+z\rangle}^{\text{th}} = 1\%$ is suppressed using active reset heralding. The coherence times T_1 and T_2 are measured using standard relaxation and Ramsey interferometry techniques. While the input and output lines introduce scaling factors between the fields $\langle \hat{b}_{\text{in}} \rangle$, $\langle \hat{b}_{\text{out}} \rangle$ and the fields that we actually send and measure, it can be taken into account by measuring R for large enough detuning δ . This leaves Ω and Γ_c as the only fit parameters in Eq. (E1). We show $R(\delta)$ for various Rabi frequencies Ω in Fig. 7, from which we extract $\Gamma_c/2\pi = 0.383$ kHz. Due to the fluctuating qubit parameters over time, the averaging on this reflection measurement is interleaved with recalibration measurements of the qubit parameters. The reflection measurement has been performed in another cool-down than the experiments discussed in the main text.

Appendix F: Qubit Purcell decay through the readout resonator

Even though there is a Purcell filter, the qubit is also coupled to the second transmission line via its Purcell decay Γ_P through the readout resonator that we estimate here. By comparing the Rabi rates $\Omega_1 = 2\sqrt{\Gamma_c} b_{\text{in},1}$ and $\Omega_2 = 2\sqrt{\Gamma_P} b_{\text{in},2}$ from driving the qubit through the "qubit port" or the "readout port" respectively, and considering the different attenuations of the two input lines, we extract a Purcell decay through the readout resonator of $\Gamma_P/2\pi \simeq 10$ Hz $\ll \Gamma_c$. The qubit total decay rate $T_1^{-1} = 2\pi \cdot 6.4$ kHz $\gg \Gamma_c \gg \Gamma_P$ is thus not limited by its couplings to the microwave transmission lines. Moreover, due to the diplexer (see Fig. 4), the output line only amplifies signals coming from Γ_c and not the one from Γ_P .

Appendix G: Simulations

The simulations are implemented with the QuantumOptics.jl library in Julia simulating the master equation evolution of the qubit under the different drives and feedback. In the simulations, only the Hilbert space of the qubit is considered. The extracted work is computed from the qubit density matrix as $\frac{P(t)}{\hbar\omega_q} = \frac{\Omega}{2} \langle \hat{\sigma}_x(t) \rangle$ during the Rabi driving pulse. The whole time evolution of the pulse sequence of N_c cycles is computed as described in Fig. 1.c).

For the dispersive readout pulse, it is simplified and decomposed into three steps: first, a free evolution during $t_{\text{int}}/2$, then an instantaneous projection over the states $|-z\rangle$ or $|+z\rangle$ followed again by a free evolution during $t_{\text{int}}/2$. The simulations also incorporate imperfections such as an assignment error of 0.4% in the readout and

the qubit thermalization to a 1% population.

Appendix H: Extracted work as a function of cycle number

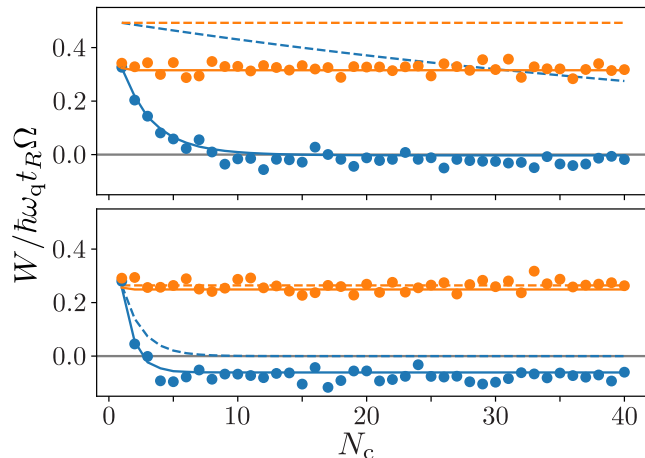


FIG. 8. Dots: normalized extracted work $W/\hbar\omega_q t_R \Omega$ of the engine in orange and of the open-loop configuration (blue) as a function of cycle number N_c for $t_R = 8 \mu\text{s}$ and $\Omega/2\pi = 3.4 \text{ kHz}$ (top) or $\Omega/2\pi = 20.2 \text{ kHz}$ (bottom). Dash lines are the analytical extracted work $W^{(N_c)} = \frac{\hbar\omega_q\theta}{2} \cos^{N_c}(\theta)$ while solid lines are simulations.

We measure the extracted work per cycle W as a function of cycle number N_c . In the engine configuration, the extracted work is as intended, independent of the cycle number (Fig. 8). However, the qubit's imperfections modify the amount of extractable work for a given t_R and Ω . In the open-loop configuration, we observe a much faster decay of the extracted work than the expected decrease $W^{(N_c)} = \frac{\hbar\omega_q\theta}{2} \cos^{N_c}(\theta)$ for a dissipationless qubit. In both the engine and open-loop configuration, the simulations fit well with the extracted work.

Appendix I: Average per cycle extracted work in open-loop configuration

Due to finite dissipation, the Zeno limit $\theta \rightarrow 0$, where work can be extracted even in the open-loop configuration, can still be approached but is less pronounced (see Fig. 9). Without dissipation, the extracted work tends to zero in the steady state (for a large cycle number $N_c \rightarrow +\infty$) except for the Zeno limit $\theta \rightarrow 0$. When considering dissipation, a finite non-zero work can still be extracted in the steady state. This work can be positive or negative depending on the Rabi parameters Ω and t_R for a given amount of dissipation.

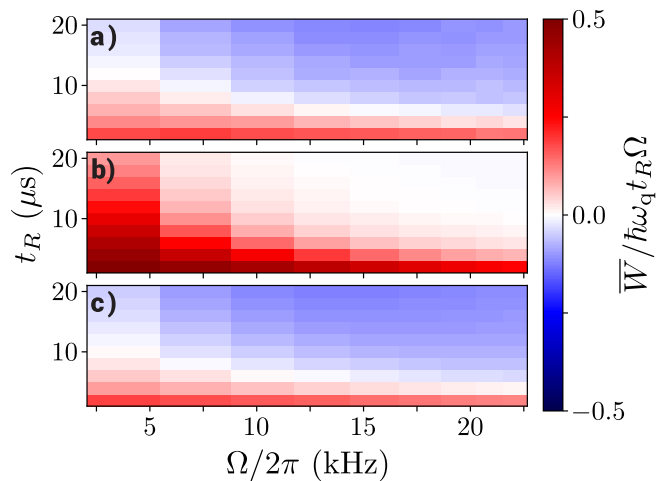


FIG. 9. Normalized extracted work $\bar{W}/\hbar\omega_q t_R \Omega$ averaged over the first 40 cycles in case of open-loop configuration, measured in a), analytical in b) and simulated in c), as a function of duration t_R and amplitude Ω .

Appendix J: Qubit parameters stability

We have observed that the qubit parameters were not fully stable over time. Through repeated relaxation and Ramsey interferometry measurements over time, we extract the qubit parameters ω_q , T_1 and T_2 histograms.

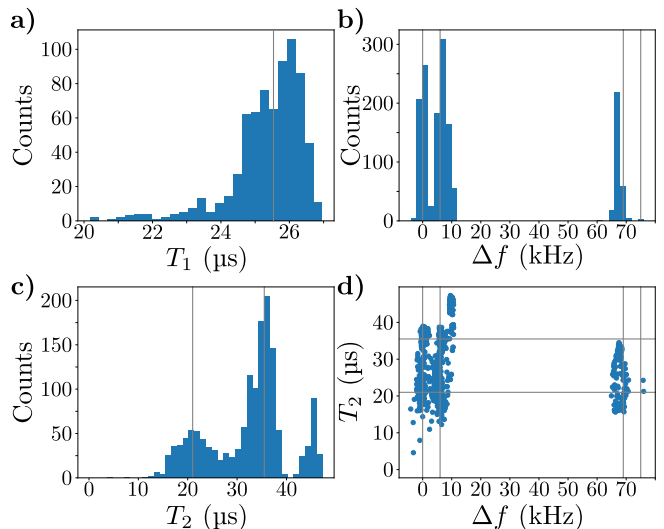


FIG. 10. Qubit parameters instability. Histograms of T_1 in a), Δf in b) and T_2 in c). In d), scatter plot of T_2 as a function of Δf . The different sets are spaced several days up to weeks apart

Different distributions could be noticed in the qubit ω_q and T_2 , that we attribute to the coupling to parasitic two-level systems [46]. In Fig. 10 are shown the qubit parameters extracted from compiled data of different sets of relaxation and Ramsey measurements taken at a rate of approximately 1 min^{-1} . The different sets are spaced

several days up to weeks apart and were performed in

the same cool-down as the experiments discussed in the main text.

-
- [1] L. M. Cangemi, C. Bhadra, and A. Levy, Quantum engines and refrigerators, *Physics Reports* **1087**, 1 (2024), quantum engines and refrigerators.
- [2] C. Elouard, D. A. Herrera-Martí, M. Clusel, and A. Auffèves, The role of quantum measurement in stochastic thermodynamics, *npj Quantum Information* **3**, 1 (2017).
- [3] S. Rogers and A. N. Jordan, Postselection and quantum energetics, *Phys. Rev. A* **106**, 052214 (2022).
- [4] M. H. Mohammady, Classicality of the heat produced by quantum measurements, *Phys. Rev. A* **104**, 062202 (2021).
- [5] X. Linpeng, N. Piccione, M. Maffei, L. Bresque, S. P. Prasad, A. N. Jordan, A. Auffèves, and K. W. Murch, Quantum energetics of a non-commuting measurement, [arXiv:2311.13634](https://arxiv.org/abs/2311.13634) (2023).
- [6] A. Solfanelli, L. Buffoni, A. Cuccoli, and M. Campisi, Maximal energy extraction via quantum measurement, *Journal of Statistical Mechanics: Theory and Experiment* **2019**, 094003 (2019).
- [7] A. Auffèves, A short story of quantum and information thermodynamics, *SciPost Phys. Lect. Notes*, 27 (2021).
- [8] A. N. Jordan, C. Elouard, and A. Auffèves, Quantum measurement engines and their relevance for quantum interpretations, *Quantum Studies: Mathematics and Foundations* **7**, 203 (2020).
- [9] K. Brandner, M. Bauer, M. T. Schmid, and U. Seifert, Coherence-enhanced efficiency of feedback-driven quantum engines, *New Journal of Physics* **17**, 065006 (2015).
- [10] C. Elouard, D. Herrera-Martí, B. Huard, and A. Auffèves, Extracting work from quantum measurement in maxwell's demon engines, *Phys. Rev. Lett.* **118**, 260603 (2017).
- [11] C. Elouard and A. N. Jordan, Efficient Quantum Measurement Engines, *Physical Review Letters* **120**, 260601 (2018).
- [12] Y. Wang, S. Xia, J. Chen, J. Chen, and S. Su, Conditional control of measurement-driven machines, *Physics Letters A* **493**, 129243 (2024).
- [13] J. Yi, P. Talkner, and Y. W. Kim, Single-temperature quantum engine without feedback control, *Phys. Rev. E* **96**, 022108 (2017).
- [14] X. Ding, J. Yi, Y. W. Kim, and P. Talkner, Measurement-driven single temperature engine, *Phys. Rev. E* **98**, 042122 (2018).
- [15] S. Su, Z. Lin, and J. Chen, Thermal divergences of quantum measurement engine, *Journal of Applied Physics* **133** (2023).
- [16] S. K. Manikandan, C. Elouard, K. W. Murch, A. Auffèves, and A. N. Jordan, Efficiently fueling a quantum engine with incompatible measurements, *Phys. Rev. E* **105**, 044137 (2022).
- [17] T. Opatrný, A. Misra, and G. Kurizki, Work generation from thermal noise by quantum phase-sensitive observation, *Phys. Rev. Lett.* **127**, 040602 (2021).
- [18] G. Manzano and R. Zambrini, Quantum thermodynamics under continuous monitoring: A general framework, *AVS Quantum Science* **4**, 025302 (2022).
- [19] L. P. Bettmann, M. J. Kewming, and J. Goold, Thermodynamics of a continuously monitored double-quantum-dot heat engine in the repeated interactions framework, *Phys. Rev. E* **107**, 044102 (2023).
- [20] N. Behzadi, Quantum engine based on general measurements, *Journal of Physics A: Mathematical and Theoretical* **54**, 015304 (2020).
- [21] T. Purves and A. J. Short, Channels, measurements, and postselection in quantum thermodynamics, *Phys. Rev. E* **104**, 014111 (2021).
- [22] L. Buffoni, A. Solfanelli, P. Verrucchi, A. Cuccoli, and M. Campisi, Quantum Measurement Cooling, *Physical Review Letters* **122**, 070603 (2019).
- [23] L. Bresque, P. A. Camati, S. Rogers, K. Murch, A. N. Jordan, and A. Auffèves, Two-Qubit Engine Fueled by Entanglement and Local Measurements, *Physical Review Letters* **126**, 120605 (2021).
- [24] M. F. Anka, T. R. de Oliveira, and D. Jonathan, Measurement-based quantum heat engine in a multilevel system, *Phys. Rev. E* **104**, 054128 (2021).
- [25] J.-s. Yan and J. Jing, Charging by quantum measurement, *Phys. Rev. Appl.* **19**, 064069 (2023).
- [26] K. Wang, R. Xia, L. Bresque, and P. Xue, Experimental demonstration of a quantum engine driven by entanglement and local measurements, *Phys. Rev. Res.* **4**, L032042 (2022).
- [27] N.-N. Wang, H. Cao, C. Zhang, X.-Y. Xu, B.-H. Liu, Y.-F. Huang, C.-F. Li, and G.-C. Guo, Experimental demonstration of quantum cooling engine powered by entangled measurement, [arXiv:2302.09948](https://arxiv.org/abs/2302.09948) (2023).
- [28] V. F. Lisboa, P. R. Dieguez, J. R. Guimarães, J. F. G. Santos, and R. M. Serra, Experimental investigation of a quantum heat engine powered by generalized measurements, *Phys. Rev. A* **106**, 022436 (2022).
- [29] P. R. Dieguez, V. F. Lisboa, and R. M. Serra, Thermal devices powered by generalized measurements with indefinite causal order, *Phys. Rev. A* **107**, 012423 (2023).
- [30] N. Cottet, S. Jezouin, L. Bretheau, P. Campagne-Ibarcq, Q. Ficheux, J. Anders, A. Auffèves, R. Azouit, P. Rouchon, and B. Huard, Observing a quantum maxwell demon at work, *Proceedings of the National Academy of Sciences* **114**, 7561 (2017).
- [31] M. Naghiloo, J. J. Alonso, A. Romito, E. Lutz, and K. W. Murch, Information gain and loss for a quantum maxwell's demon, *Phys. Rev. Lett.* **121**, 030604 (2018).
- [32] Y. Masuyama, K. Funo, Y. Murashita, A. Noguchi, S. Kono, Y. Tabuchi, R. Yamazaki, M. Ueda, and Y. Nakamura, Information-to-work conversion by maxwell's demon in a superconducting circuit quantum electrodynamic system, *Nature Communications* **9**, 1291 (2018).
- [33] M. Naghiloo, D. Tan, P. M. Harrington, J. J. Alonso, E. Lutz, A. Romito, and K. W. Murch, Heat and work along individual trajectories of a quantum bit, *Phys. Rev. Lett.* **124**, 110604 (2020).
- [34] X. Song, M. Naghiloo, and K. Murch, Quantum process

- inference for a single-qubit maxwell demon, *Phys. Rev. A* **104**, 022211 (2021).
- [35] J. P. Pekola and B. Karimi, Colloquium: Quantum heat transport in condensed matter systems, *Rev. Mod. Phys.* **93**, 041001 (2021).
- [36] J. Stevens, D. Szombati, M. Maffei, C. Elouard, R. Assouly, N. Cottet, R. Dassonneville, Q. Ficheux, S. Zepetzauer, A. Bienfait, A. N. Jordan, A. Auffèves, and B. Huard, Energetics of a single qubit gate, *Phys. Rev. Lett.* **129**, 110601 (2022).
- [37] X. Linpeng, L. Bresque, M. Maffei, A. N. Jordan, A. Auffèves, and K. W. Murch, Energetic cost of measurements using quantum, coherent, and thermal light, *Phys. Rev. Lett.* **128**, 220506 (2022).
- [38] M. Spiecker, P. Paluch, N. Gosling, N. Drucker, S. Matityahu, D. Gusenkova, S. Günzler, D. Rieger, I. Takmakov, F. Valenti, P. Winkel, R. Gebauer, O. Sander, G. Catelani, A. Shnirman, A. V. Ustinov, W. Wernsdorfer, Y. Cohen, and I. M. Pop, Two-level system hyperpolarization using a quantum szilard engine, *Nature Physics* **19**, 1320 (2023).
- [39] E. Gümüş, D. Majidi, D. Nikolić, P. Raif, B. Karimi, J. T. Peltonen, E. Scheer, J. P. Pekola, H. Courtois, W. Belzig, and C. B. Winkelmann, Calorimetry of a phase slip in a josephson junction, *Nature Physics* **19**, 196 (2023).
- [40] S. Erdamar, M. Abbasi, B. Ha, W. Chen, J. Muldoon, Y. Joglekar, and K. W. Murch, Constraining work fluctuations of non-hermitian dynamics across the exceptional point of a superconducting qubit, *Phys. Rev. Res.* **6**, L022013 (2024).
- [41] C. W. Gardiner and M. J. Collett, Input and output in damped quantum systems: Quantum stochastic differential equations and the master equation, *Phys. Rev. A* **31**, 3761 (1985).
- [42] U. Vool and M. Devoret, Introduction to quantum electromagnetic circuits, *International Journal of Circuit Theory and Applications* **45**, 897 (2017).
- [43] A. A. Clerk, M. H. Devoret, S. M. Girvin, F. Marquardt, and R. J. Schoelkopf, Introduction to quantum noise, measurement, and amplification, *Reviews of Modern Physics* **82**, 1155 (2010).
- [44] N. Cottet, *Energy and information in fluorescence with superconducting circuits*, PhD Thesis, ENS Paris (2018).
- [45] C. Macklin, K. O'Brien, D. Hover, M. E. Schwartz, V. Bolkhovskiy, X. Zhang, W. D. Oliver, and I. Siddiqi, A near-quantum-limited Josephson traveling-wave parametric amplifier, *Science* **350**, 307 (2015).
- [46] C. Muller, J. H. Cole, and J. Lisenfeld, Towards understanding two-level-systems in amorphous solids: insights from quantum circuits, *Reports on Progress in Physics* **82**, 124501 (2019).
- [47] A. Vepsäläinen, R. Winik, A. H. Karamlou, J. Braumüller, A. D. Paolo, Y. Sung, B. Kannan, M. Kjaergaard, D. K. Kim, A. J. Melville, B. M. Niedzielski, J. L. Yoder, S. Gustavsson, and W. D. Oliver, Improving qubit coherence using closed-loop feedback, *Nature Communications* **13**, 1932 (2022).
- [48] C. Elouard and M. H. Mohammady, Work, Heat and Entropy Production Along Quantum Trajectories, in *Thermodynamics in the Quantum Regime* (Springer, Cham, Switzerland, 2019) pp. 363–393.
- [49] K. Prech and P. P. Potts, Quantum Fluctuation Theorem for Arbitrary Measurement and Feedback Schemes, *Physical Review Letters* **133**, 140401 (2024).
- [50] Y. Hasegawa, Quantum Thermodynamic Uncertainty Relation for Continuous Measurement, *Physical Review Letters* **125**, 050601 (2020).
- [51] D. Reiche, J.-T. Hsiang, and B.-L. Hu, Quantum Thermodynamic Uncertainty Relations, Generalized Current Fluctuations and Nonequilibrium Fluctuation–Dissipation Inequalities, *Entropy* **24**, 1016 (2022).
- [52] A. Maity and A. Ghoshal, Violation of the Thermodynamic Uncertainty Relation in Quantum Collisional Models, *arXiv:2501.00627* (2024).
- [53] S. V. Moreira, M. Radaelli, A. Candeloro, F. C. Binder, and M. T. Mitchison, Precision bounds for multiple currents in open quantum systems, *ArXiv e-prints* **10.48550/arXiv.2411.09088** (2024).
- [54] A. Eddins, J. M. Kreikebaum, D. M. Toyli, E. M. Levenson-Falk, A. Dove, W. P. Livingston, B. A. Levitan, L. C. G. Govia, A. A. Clerk, and I. Siddiqi, High-efficiency measurement of an artificial atom embedded in a parametric amplifier, *Phys. Rev. X* **9**, 011004 (2019).
- [55] R. Dassonneville, R. Assouly, T. Peronin, P. Rouchon, and B. Huard, Number-Resolved Photocounter for Propagating Microwave Mode, *Physical Review Applied* **14**, 044022 (2020).
- [56] R. Lescanne, S. Deléglise, E. Albertinale, U. Réglade, T. Capelle, E. Ivanov, T. Jacqmin, Z. Leghtas, and E. Flurin, Irreversible qubit-photon coupling for the detection of itinerant microwave photons, *Phys. Rev. X* **10**, 021038 (2020).
- [57] L. Balembois, J. Travesedo, L. Pallegoix, A. May, E. Billaud, M. Villiers, D. Estève, D. Vion, P. Bertet, and E. Flurin, Cyclically operated microwave single-photon counter with sensitivity of 10^{-22} W/ $\sqrt{\text{Hz}}$, *Phys. Rev. Appl.* **21**, 014043 (2024).
- [58] A. Gunyhó, K. Kohvakka, Q.-M. Chen, J.-P. Girard, R. Kokkonen, W. Liu, and M. Möttönen, Zeptojoule calorimetry, *arXiv:2412.14079* (2024).
- [59] M. Xia, C. Zhou, C. Liu, P. Patel, X. Cao, P. Lu, B. Mesits, M. Mucci, D. Gorski, D. Pekker, and M. Hatridge, Fast superconducting qubit control with subharmonic drives, *arXiv:2306.10162* (2023).
- [60] O. Abah, R. Puebla, A. Kiely, G. D. Chiara, M. Paternostro, and S. Campbell, Energetic cost of quantum control protocols, *New Journal of Physics* **21**, 103048 (2019).
- [61] J. Gea-Banacloche, Minimum energy requirements for quantum computation, *Phys. Rev. Lett.* **89**, 217901 (2002).
- [62] J. Ikonen, J. Salmilehto, and M. Möttönen, Energy-efficient quantum computing, *npj Quantum Information* **3**, 1 (2017).
- [63] S. Silva Pratapsi, P. H. Huber, P. Barthel, S. Bose, C. Wunderlich, and Y. Omar, Classical half-adder using trapped-ion quantum bits: Toward energy-efficient computation, *Applied Physics Letters* **123**, 154003 (2023).
- [64] F. Góis, M. Pezzutto, and Y. Omar, Towards energetic quantum advantage in trapped-ion quantum computation, *arXiv:2404.11572* (2024).
- [65] M. Fellous-Asiani, J. H. Chai, Y. Thonnart, H. K. Ng, R. S. Whitney, and A. Auffèves, Optimizing resource efficiencies for scalable full-stack quantum computers, *PRX Quantum* **4**, 040319 (2023).
- [66] D. Sank, Z. Chen, M. Khezri, J. Kelly, R. Barends, B. Campbell, Y. Chen, B. Chiaro, A. Dunsworth, A. Fowler, E. Jeffrey, E. Lucero, A. Megrant, J. Mutus, M. Neeley, C. Neill, P. J. J. O'Malley, C. Quin-

- tana, P. Roushan, A. Vainsencher, T. White, J. Wenner, A. N. Korotkov, and J. M. Martinis, Measurement-induced state transitions in a superconducting qubit: Beyond the rotating wave approximation, *Phys. Rev. Lett.* **117**, 190503 (2016).
- [67] R. Lescanne, L. Verney, Q. Ficheux, M. H. Devoret, B. Huard, M. Mirrahimi, and Z. Leghtas, Escape of a driven quantum Josephson circuit into unconfined states, *Phys. Rev. Appl.* **11**, 014030 (2019).
- [68] R. Shillito, A. Petrescu, J. Cohen, J. Beall, M. Hauru, M. Ganahl, A. G. Lewis, G. Vidal, and A. Blais, Dynamics of transmon ionization, *Phys. Rev. Appl.* **18**, 034031 (2022).
- [69] C. Lledó, R. Dassonneville, A. Moulinas, J. Cohen, R. Shillito, A. Bienfait, B. Huard, and A. Blais, Cloaking a qubit in a cavity, *Nature Communications* **14**, 6313 (2023).
- [70] P. Campagne-Ibarcq, E. Flurin, N. Roch, D. Darson, P. Morfin, M. Mirrahimi, M. H. Devoret, F. Mallet, and B. Huard, Persistent control of a superconducting qubit by stroboscopic measurement feedback, *Phys. Rev. X* **3**, 021008 (2013).